

Photochemistry of polycyclic aromatic hydrocarbons in cosmic water ice

I. Mid-IR spectroscopy and photoproducts

J. Bouwman¹, A. L. Mattioda², H. Linnartz¹, and L. J. Allamandola²

¹ Raymond and Beverly Sackler Laboratory for Astrophysics, Leiden Observatory, Leiden University, PO Box 9513, 2300 RA Leiden, The Netherlands

e-mail: bouwman@strw.leidenuniv.nl

² NASA-Ames Research Center, Space Science Division, Mail Stop 245-6, Moffett Field, CA 94035, USA

Received 27 May 2010 / Accepted 23 September 2010

ABSTRACT

Context. Polycyclic aromatic hydrocarbons (PAHs) are known to be abundantly present in photon-dominated regions (PDRs), as evidenced by their ubiquitous mid-IR emission bands. Towards dense clouds, however, their IR emission bands are strongly suppressed. It is here where molecules are known to reside on very cold grains ($T \leq 30$ K) in the form of interstellar ices. Therefore, it is likely that non-volatile species, such as PAHs, also freeze out on grains. Such icy grains act as catalytic sites and, upon vacuum ultraviolet (VUV) irradiation, chemical reactions are initiated. In the study presented here, these reactions and the resulting photoproducts are investigated for PAH containing water ices.

Aims. The aim of this work is to monitor vacuum ultraviolet induced chemical reactions of PAHs in cosmic ice through their IR signatures, to characterize the families of species formed in these reactions, and to apply the results to astronomical observations.

Methods. Mid-infrared Fourier transform absorption spectroscopic measurements ranging from 6500 to 450 cm^{-1} are performed on freshly deposited and vacuum ultraviolet processed PAH containing cosmic H_2O ices at low temperatures.

Results. The mid-IR spectroscopy of anthracene, pyrene and benzo[ghi]perylene containing H_2O ice is reported. Band strengths of the neutral PAH modes in H_2O ice are derived. Additionally, spectra of vacuum ultraviolet processed PAH containing H_2O ices are presented. These spectra are compared to spectra measured in VUV processed PAH:argon matrix isolation studies. It is concluded that the parent PAH species is ionized in H_2O ice and that other photoproducts, mainly more complex PAH derivatives, also form. The importance of PAHs and their PAH: H_2O photoproducts in astronomical mid-infrared spectroscopic studies, in particular in the 5–8 μm region, is discussed. As a test-case, the VUV photolyzed PAH: H_2O laboratory spectra are compared to a high resolution ISO-SWS spectrum of the high-mass embedded protostar W33A and to a *Spitzer* spectrum of the low-mass Young Stellar Object (YSO) RNO 91. For these objects, an upper limit of 2–3% with respect to H_2O ice is derived for the contribution of PAHs and PAH: H_2O photoproducts to the absorbance in the 5–8 μm region towards these objects.

Key words. astrochemistry – molecular processes – methods: laboratory – techniques: spectroscopic – infrared: ISM – ISM: abundances

1. Introduction

Polycyclic aromatic hydrocarbons (PAHs) are known to be abundantly present in photon-dominated regions (PDRs) (Peeters et al. 2004; van Dishoeck 2004; Tielens 2008). The evidence for the ubiquity of astronomical PAHs is the widespread, well-known family of prominent emission bands at 3.28, 6.2, 7.6, 8.6, and 11.2 μm (3050, 1610, 1300, 1160, and 890 cm^{-1}) associated with many, if not most, galactic and extragalactic objects (Smith et al. 2007; Draine & Li 2007). These bands dominate the mid-IR emission spectrum because of an intrinsically high efficiency of the fluorescent process and are most easily detected in regions where individual gas-phase PAH molecules (both neutrals and ions) become highly vibrationally excited by the ambient UV-VIS-NIR radiation field (Mattioda et al. 2005a; Li & Draine 2002). They then energetically relax by emission of IR photons at frequencies corresponding to fundamental vibrational modes, resulting in these well known emission spectra.

PAHs and related aromatic materials are expected to be present both in optically thin, diffuse regions of the ISM and in dense environments. In dense regions, however, the highly

efficient PAH fluorescence is found to be quenched. There are two reasons for this. First, the radiation which pumps the emission tapers off with extinction into dense regions, and second, in cold molecular clouds PAHs can serve as nucleation sites on which other species condense. In this way, neutral and/or charged PAHs can agglomerate to form (charged) PAH clusters, or very small grains (VSGs) (e.g., Allamandola et al. 1989; Rapacioli et al. 2006). The VSGs can, subsequently, freeze out on grains or serve as nucleation sites for small molecules forming ice covered VSGs. Individual PAHs can also efficiently condense onto dust grains as “guest molecules” in icy grain mantles, much as is the case for most other smaller interstellar molecules (e.g., Sandford & Allamandola 1993). Vibrational energy of a PAH molecule which is part of a larger dust particle, either as a nucleation center or guest in a water-rich ice, efficiently dissipates into the phonon modes of the solid material on a time-scale orders of magnitude shorter than required to emit an IR photon (Allamandola et al. 1985, 1989). Consequently, in dark, dense regions, PAHs and PAH derivatives are expected to give rise to IR absorption bands, not to emission features.

There are several lines of evidence that support the presence of PAHs in dense molecular clouds. Aromatics in primitive meteorites and interplanetary dust particles contain deuterium enrichments that are best explained by an interstellar cloud heritage (e.g., Sandford 2002, and references therein). In addition, very weak absorption features attributed to aromatic hydrocarbons have been observed in the IR absorption spectra of objects embedded in dense clouds. These include a band near $3.3 \mu\text{m}$ (3030 cm^{-1}) (Smith et al. 1989; Sellgren et al. 1995; Brooke et al. 1999; Chiar et al. 2000), and bands near $6.2 \mu\text{m}$ (1600 cm^{-1}) (Chiar et al. 2000) and $11.2 \mu\text{m}$ (890 cm^{-1}) (Bregman et al. 2000). These very weak features are severely blended with much stronger H_2O ice bands, consistent with the number of PAH molecules relative to the number of H_2O molecules along these lines of sight on the order of a few percent. So far, it has proven difficult to unambiguously interpret these absorption features in spite of the fact that there is a growing database of theoretically calculated and laboratory measured IR absorption spectra of both neutral and ionized PAHs in inert matrices (e.g., Szczepanski & Vala 1993; Szczepanski et al. 1993a,b, 1995a,b; Hudgins et al. 1994; Hudgins & Allamandola 1995a, 1997; Langhoff 1996; Mattioda et al. 2005b; Bauschlicher et al. 2009, 2010, and references therein). Unfortunately, these spectra cannot be used directly to compare with PAHs in H_2O -rich ices, as rare gas matrix spectra will be different. Intermolecular interactions perturb the molecular vibrational energy levels, influencing IR band positions, widths, profiles, and intrinsic strengths. Consequently, it has not yet been possible to properly evaluate astronomical solid state PAH features, mainly because the corresponding laboratory data of *realistic ice analogs* are lacking.

Therefore, in the Astrochemistry Laboratory at NASA Ames Research Center a program to measure the IR spectra of PAHs in water ices was started. Earlier work focused on the IR band positions, band widths, and relative band strengths of neutral PAHs (Sandford et al. 2004; Bernstein et al. 2005a,b). More recently, an exploratory study of the effects of vacuum ultraviolet (VUV) photolysis on several PAH: H_2O ice mixtures was carried out (Bernstein et al. 2007). Unfortunately, at concentrations that are most appropriate for dense clouds, PAH bands are swamped in the mid-IR by overlapping H_2O ice bands and it has proven difficult to put these IR-only data on a solid quantitative footing. This situation has recently changed thanks to the development of a new apparatus at the Sackler Laboratory for Astrophysics at Leiden University which allows one to track the in situ, VUV photochemistry of low concentration PAH: H_2O ices (Bouwman et al. 2009, 2010a, in prep., 2010b) using optical (i.e. electronic) spectroscopy. This approach makes it possible to simultaneously follow the VUV driven kinetic behavior of the neutral parent PAH and photoproducts on millisecond timescales with a concentration precision on the order of a few percent. Using this approach, it was possible to characterize the VUV photochemistry of four PAHs anthracene, pyrene, benzo[ghi]perylene, and coronene in water ice at various concentrations and ice temperatures. This is described in detail in part II of this paper series (Bouwman et al. 2010a, in prep.). The mid-IR study presented here is partially based on the quantitative results derived in the optical work.

This paper is laid out as follows. After the experimental technique is described in Sect. 2, the results are presented in Sects. 3, 4 and 5. These include band profiles and band strengths for neutral anthracene, pyrene and benzo[ghi]perylene in H_2O ice, the IR spectroscopic properties of their VUV induced photoproducts, and the visualization of photochemical processes at play

Table 1. Overview of the used ice mixtures, the PAH deposition temperatures, the resulting concentration, and the ice temperature during photolysis.

Ice (PAH:X)	T_{dep} ($^{\circ}\text{C}$)	Conc. (PAH:X)	T_{ice} (K)
Ant: H_2O	32	1:450	15
	42	1:172	15
	53	1:60	15
	71	1:11	15
	51	1:100	125
Py: H_2O	41	1:200	15
	44	1:90	15
	50	1:65	15
	51	1:70	125
Py:CO	50	1:30	15
$\text{B}_{\text{ghi}}\text{P}:\text{H}_2\text{O}$	143	1:160	15
	156	1:60	15
	152	1:110	125

during extended photolysis. In Sect. 6 we extend our findings to the general IR properties of PAHs in ices and use these data to interpret observations of ices in dense clouds towards the high-mass protostar W33A and the low-mass young stellar object RNO 91. The conclusions are summarized in Sect. 7.

2. Experimental technique

The techniques employed in this study have been described in detail previously (Hudgins et al. 1994) and the relevant details are summarized briefly. The ices are prepared by vapor co-deposition of the PAH of interest with water vapor onto a 15 K CsI window which is suspended in a high vacuum chamber ($P \leq 10^{-8}$ Torr). The PAHs anthracene (Ant, $\text{C}_{14}\text{H}_{10}$, Aldrich, 99%) and pyrene (Py, $\text{C}_{16}\text{H}_{10}$, Aldrich, 99%) are used without further purification and vaporized from heated pyrex tubes. The PAH benzo[ghi]perylene ($\text{B}_{\text{ghi}}\text{P}$, $\text{C}_{22}\text{H}_{12}$, Aldrich, 98%) is kept at a temperature of 180°C for 20 min with a cold shield blocking the deposition onto the sample window to remove most of the contaminants and is subsequently deposited in a manner similar to that for Ant and Py. Simultaneously, water vapor – milli-Q grade, further purified by three freeze-pump-thaw cycles – is admitted through an adjacent deposition tube. To prepare PAH: H_2O ices with different concentrations, the PAH deposition temperature was varied from one experiment to the other, while the water flow was kept constant. Mid-infrared spectroscopy of the PAHs Ant, Py, and $\text{B}_{\text{ghi}}\text{P}$ in water ice and for Py:CO ice as a control experiment is performed for a range of concentrations. The PAH deposition temperature, the resulting PAH concentration, and the ice temperature during photolysis are summarized in Table 1.

VUV photolysis of the sample ices is accomplished with the combined 121.6 nm Lyman- α (10.6 eV) and 160 nm (7.8 eV) molecular hydrogen emission bands from a microwave powered discharge in a flowing H_2 gas at a dynamic pressure of 150 mTorr. The VUV radiation from the lamp enters the sample chamber through a MgF_2 window. The UV photon flux of the lamp is $\sim 10^{15}$ photons $\text{cm}^{-2} \text{ s}^{-1}$ at the sample surface.

Spectra from 6500 to 450 cm^{-1} are measured with a Biorad Excalibur FTS 4000 FTIR spectrometer equipped with a KBr beamsplitter and a liquid N_2 -cooled MCT detector. Spectra are taken in optical depth ($\tau = \ln(I/I_0)$), with the background spectrum (I_0) taken on the cold sample window before sample deposition, and the spectra (I) taken after deposition and

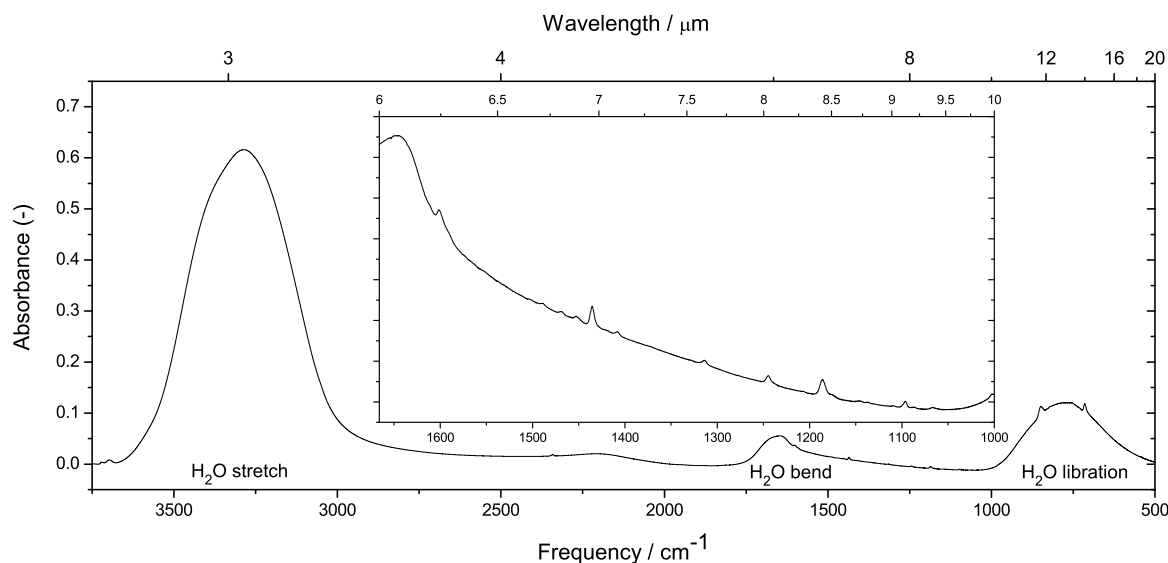


Fig. 1. A typical absorption spectrum for a pyrene:H₂O (1:90) ice mixture at 15 K. The inset shows a blow-up of that part of the spectrum (region of interest) where Py absorptions are least affected by the water modes. The water modes are labeled in the spectrum.

VUV processing of the sample. Each spectrum represents a co-addition of 512 spectra at a resolution of 0.5 cm⁻¹. This level of resolution is necessary to distinguish photoproduct bands that are close to the position of the neutral band. The number of scans was chosen to optimize both the signal-to-noise ratio as well as the time requirements for each experiment. Spectra are taken at 15 K of the freshly deposited sample and after 5, 10, 15, 30, 60, 120, and 180 min of VUV photolysis. Similar measurements are also performed on PAH:H₂O ice samples at 125 K to check for differences in photochemistry between low and high temperature photolysis experiments.

We focus on the bands in the 1650–1000 cm⁻¹ region because this is where the PAH mid-IR bands suffer the least from overlap with the strong H₂O ice features (Fig. 1). Hereafter we refer to this as the Region Of Interest (ROI). The absolute band strengths for the neutral PAH modes in H₂O ice are derived as follows. The H₂O bending and librational overtone modes are subtracted from the raw spectrum by fitting a spline function through a set of points where no PAH absorption occurs. Subsequently, the total theoretically calculated absolute intensity in the ROI is proportionally divided over the measured PAH modes in this frequency range, via:

$$A_i^{\text{exp}} = \left[\sum_{j=0}^M A_j^{\text{thy}} \right] \frac{\int_{\nu_{i,1}}^{\nu_{i,2}} \tau_{i,\nu} d\nu}{\sum_{i=0}^L \int_{\nu_{i,1}}^{\nu_{i,2}} \tau_{i,\nu} d\nu}, \quad (1)$$

where A_i^{exp} is the experimentally measured band strength of PAH mode i in H₂O ice in cm molecule⁻¹, A_j^{thy} is the theoretically calculated absolute intensity of vibrational mode j in the ROI in cm molecule⁻¹, M is the number of theoretically calculated modes in the ROI, $\tau_{i,\nu}$ is the optical depth of mode i in H₂O ice at frequency ν (cm⁻¹), L is the number of measured modes in the ROI, and $\nu_{i,1}$ and $\nu_{i,2}$ are the lower and upper integration boundaries in cm⁻¹, respectively, for absorption feature i . This method takes advantage of the fact that, although there may be band-to-band variations in the accuracy of the calculated intensity for one band, the total theoretically calculated intensity is generally accurate to within 10–20%. Here we assume that the matrix material does not substantially influence the total integrated

IR band intensity and, as will be shown later, this is only an approximation.

The PAH in H₂O concentrations are determined as follows. The optical depths (τ_ν) of the 3 μm stretching, 6 μm bending, and 13 μm libration modes of water are integrated over the frequency domain (ν in cm⁻¹) and converted into the column density (N in molecules cm⁻²), using the well known H₂O band strength values A_{band} (Hudgins et al. 1993), via:

$$N = \frac{\int \tau_\nu d\nu}{A_{\text{band}}}. \quad (2)$$

The adopted H₂O band strength values, A_{band} , are 2×10^{-16} , 1.2×10^{-17} and 3.1×10^{-17} cm molecule⁻¹ for the stretching, bending and libration mode, respectively. The H₂O column density is determined by taking the average of these three strong H₂O bands. Similarly, at least four strong bands of the PAHs under investigation are integrated and converted to column densities using the band strengths for these modes as calculated above (Eq. (1)). The average PAH column density is used to determine the concentration, which is given by the ratio of the PAH and H₂O column densities.

Comparison of the PAH:H₂O ice spectrum before photolysis to that measured after photolysis permits identification of photoproduct features, including cation absorption bands. The spectrum of the freshly deposited PAH:H₂O ice, multiplied by a factor, Y ($0 \leq Y \leq 1$), is used as a reference that is subtracted from the spectrum of the irradiated ice using the Resolutions Pro spectrometer software package provided by Biorad. The factor Y is varied until the neutral bands are removed from the spectrum. At this point, the resulting subtraction spectrum reveals *only* the photoproduct bands and the subtraction factor, Y , directly reflects the amount of neutral PAH consumed during photolysis. Additionally, the remaining contributions from the H₂O librational overtone and H₂O bending mode are subtracted by a spline function, for which points are chosen at positions where no PAH photoproduct absorptions are observed. The resulting baseline corrected spectra are used for further analysis.

The sample window on which the ices are grown was thoroughly cleaned before commencing experiments on a different PAH. Thus, the background spectrum taken of the cold sample

window before starting a series of measurements (I_0) was free of PAH absorptions. For one specific PAH, typically five individual PAH:H₂O photolysis experiments were performed for different concentrations and temperatures (Table 1), during which a residue built up, comprising unprocessed PAH, and presumably also PAH:H₂O photoproducts. After completion of the measurement series for this specific PAH, a spectrum (I) was taken of the room temperature “dirty” sample window. Subsequently, the system was cleaned and prepared for the next run. The ratio $\ln(I/I_0)$ reflects the optical depth spectrum of the non-volatile residue and is used to derive complementary information on the species formed in the ice. The non-volatile residues that built up during the Ant, Py, and B_{ghi}P measurement series are discussed in Sect. 5.

3. PAH:H₂O spectroscopy

Earlier observations (Smith et al. 1989; Sellgren et al. 1995; Brooke et al. 1999; Chiar et al. 2000; Bregman et al. 2000) indicate that the ratio of the number of PAH molecules to the number of H₂O ice molecules is small along lines of sight towards protostars in dense clouds. Based on these observations, we deduce that this number seems to be on the order of a few percent. In a very careful study, Sellgren et al. (1995) reported the optical depth of the 3.25 μm aromatic C–H stretch band towards Mon R2/IRS 3 as 0.045 with a *FWHM* of 75 cm^{-1} . These values are similar to the range of values reported by Bregman & Temi (2001) towards other deeply embedded protostars. For the purposes of this analysis, we use the results from Sellgren et al. (1995). Similar conclusions can be drawn using the observations from these other lines of sight.

Using the standard equation to determine the column density of absorbers along a given line of sight:

$$N = \frac{\tau \times FWHM}{A}, \quad (3)$$

with the *FWHM* in cm^{-1} and an A value of 2.5×10^{-18} cm per aromatic C–H bond (e.g. Joblin et al. 1994; Bauschlicher et al. 2008) yields 1.4×10^{18} aromatic C–H groups per cm^2 along the line of sight to Mon R2/IRS 3. Astronomical PAHs are thought to range in size from roughly C₂₅ to well over C₁₀₀. Reasonable formulae for such sized species are C₃₂H₁₅ and C₁₃₀H₂₈. To take this into account, we estimate that the “average” number of aromatic C–H bonds per astronomical PAH is 25. Dividing the column density of aromatic C–H bonds towards Mon R2/IRS 3 (1.4×10^{18}) by 25 yields the PAH column density, 5.4×10^{16} PAHs cm^{-2} . Likewise, for Mon R2/IRS 3 we derive 3.3×10^{18} H₂O ice molecules cm^{-2} from the O–H stretch band in Smith et al. (1989). Thus, the PAH/H₂O ice ratio along this line of sight is $5.4 \times 10^{16} / 3.3 \times 10^{18} = 0.016$, or 2%.

Figure 1 presents the 3750–500 cm^{-1} spectrum of a Py:H₂O (1:90) ice at 15 K, which clearly shows that the H₂O ice bands dominate the spectrum at these concentrations. In agreement with earlier findings on other PAHs at concentrations of a few percent in H₂O ice, the CH–stretch band near 3030 cm^{-1} (3.3 μm) is nearly imperceptible, while the strong C–H out-of-plane bending bands between 900–500 cm^{-1} (11–20 μm) suffer from severe blending with the H₂O ice libration mode (Sandford et al. 2004; Bernstein et al. 2005a). This makes PAH bands between 1650–1000 cm^{-1} (~6.06–10 μm , the ROI) the most promising to study PAH:H₂O photochemistry, and to identify astronomical PAHs and PAH related photoproduct species in interstellar ices.

The spectroscopy of PAH:H₂O ice samples is discussed for Ant, Py, and B_{ghi}P and compared to available PAH matrix isolation data. In Fig. 2 typical baseline corrected spectra of the three neutral PAHs in argon (trace A) are plotted together with the spectra of the neutral PAH:H₂O (trace B) ice (~1:60). The spectra are normalized to the strongest absorptions in the ROI. Clearly, the absorption bands are much broader in water ice compared to the argon matrix data, causing some of the absorption bands to overlap. Furthermore, the relative intensities of the bands differ for an argon or H₂O environment. The band positions and integrated absorbances relative to that of the strongest PAH absorption are listed in Table 2 for Ant, Py and B_{ghi}P in H₂O ice and in an argon matrix (Hudgins & Sandford 1998a). The corresponding Density Functional Theory (DFT) peak positions taken from Langhoff (1996) are given as well. The absolute band strengths for PAHs in H₂O ice, calculated under the assumptions described in Sect. 2, are also listed in Table 2. Within the errors, the *FWHM*, relative intensity, and position of the band maximum of absorptions of the three species studied here are found to be independent of concentration and temperature for the values listed in Table 1, even for the two most extreme Ant:H₂O ice concentrations (1:11 and 1:450). Thus, although we cannot fully exclude the presence of PAH aggregates in the ice, there is no spectral evidence for such species.

4. PAH ice photochemistry

All PAH:H₂O ice samples listed in Table 1 are VUV irradiated for 5, 10, 15, 30, 60, 120, and 180 min. Mid-IR spectra are taken after each VUV dose to look for changes in the spectrum. Spline baseline corrected spectra after 5 min of VUV irradiation of the Ant, Py, and B_{ghi}P containing H₂O ice samples with a mixing ratio of ~1:60 are shown in trace (D) of Fig. 2. In this figure, the spectra are compared to those of the corresponding PAH⁺ species produced and trapped in solid argon (trace C). Comparison of the traces (D) and (B) in Fig. 2 shows that new absorptions arise upon photolysis of the PAH:H₂O mixtures. The photoproduct features are, however, heavily blended with those of the remaining neutral PAH. To overcome this, spectra of freshly deposited PAHs are subtracted from their VUV photolyzed counterparts with a subtraction factor, Y , as described in Sect. 2. Subsequently, the contribution by the librational overtone and the H₂O bending mode are removed by fitting and subtracting a spline function. The resulting spectra are shown in trace (E) of Fig. 2 and show photoproducts only. The spectra are again scaled to the strongest absorption in the ROI. It has to be noted here, that the absorption bands of the photoproducts after 5 min of VUV irradiation are rather small compared to those of the neutral bands, as can be seen by comparing trace (B) and (D) from Fig. 2. While band intensities grow with longer irradiation time, the combination of spectral overlap and different photoproduct band growths and losses makes it difficult to track the precise photochemistry at longer photolysis times. This is discussed later in Sect. 4.2.

It is clear from Table 2 that the relative PAH band strengths in H₂O ice are different from those in an argon matrix, but the PAH cation band strengths measured in argon have to be used for further analysis, since band strength values for PAH cation vibrational modes in H₂O ice cannot be reliably determined for two reasons. First, the appearance of bands other than cation absorptions after 5 min of photolysis points out that there is no one-to-one conversion of the neutral PAH to the cation and, thus, the column density of used up neutral PAH molecules cannot be used as a reliable column density for cations in the ice on which

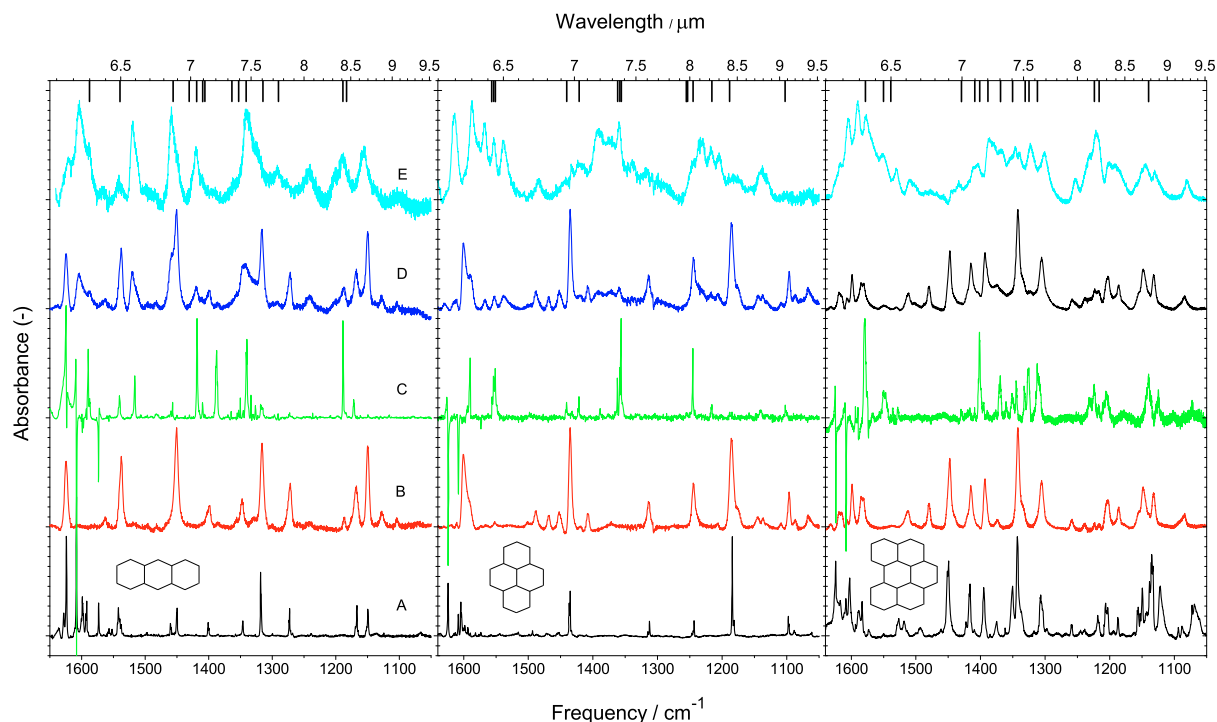


Fig. 2. From left to right the 1640 to 1050 cm^{-1} spectra of the PAHs anthracene, pyrene, and benzo[ghi]perylene considered are shown here. **A)** Spectra of the neutral PAH in argon; **B)** spectra of the neutral PAH in water ice; **C)** spectra of the PAH cation in argon; **D)** spectra of the PAH:H₂O mixture after 5 min of in situ VUV photolysis; and **E)** spectra showing *only* the photoproduct features that appear after 5 min of in situ VUV photolysis of the PAH:H₂O ice (spectrum “D” – $Y \times “B”$). The tick marks connected to the top axis indicate the positions of PAH⁺ features measured in argon. The PAH:matrix concentrations and temperatures for the spectra shown in A and B are: Ant:Ar < 1:1000, 10 K; Py:Ar < 1:1000, 10 K; B_{ghi}P:Ar < 1:1000, 10 K and Ant:H₂O = 1:60, 15 K; Py:H₂O = 1:65, 15 K; B_{ghi}P:H₂O = 1:60, 15 K. Argon matrix spectra of neutral Ant and Py are reproduced from [Hudgins & Sandford \(1998a\)](#), neutral B_{ghi}P from [Hudgins & Sandford \(1998b\)](#), ionized Ant from [Hudgins & Allamandola \(1995b\)](#), and ionized Py and B_{ghi}P from [Hudgins & Allamandola \(1995a\)](#).

to base a further band strength analysis. Secondly, spectral congestion and ill-defined baselines make it hard to obtain accurate band areas of photoproduct bands in irradiated mixtures. This choice induces additional errors in the absolute PAH⁺ column density that can be as high as a factor of two.

4.1. PAH:H₂O photoproducts

VUV photoprocessed PAH containing H₂O ices spectra exhibit a set of broad absorption features (see trace E of Fig. 2). As with the neutral PAHs, the absorption profiles of PAH photoproducts in H₂O ice are much broader than those in an argon matrix (trace C). These PAH:H₂O photoproduct absorption bands are decomposed by multiple Gaussian fits and the peak positions of these bands are listed together with PAH⁺ absorptions and band strengths measured in argon in Table 3. The solid lines along the top margin indicate the PAH cation band positions in Ar ([Hudgins & Allamandola 1995a,b](#)). The photoproduct bands that fall within 10 cm^{-1} of these features are assigned to the PAH⁺ bands in H₂O. Some of the newly formed absorption bands, however, occur at positions where no corresponding PAH⁺ band is found in argon. These absorption bands reflect additional chemical reactions already at play in the early photolysis of PAH:H₂O ices.

It is well known that H₂O molecules photodissociate into radicals (H+OH) and that these radicals are mobile within H₂O ice, even at low temperatures ([Andersson & van Dishoeck 2008](#); [Öberg et al. 2009](#)). At the concentrations under consideration here, it is therefore likely that these and other photoproducts

react with the PAHs, forming more complex aromatic species containing functional groups that give rise to different peak positions in the mid-IR spectra (see also [Bouwman et al. 2010b](#) and the discussion in [Gudipati & Allamandola 2006](#)). While infrared spectroscopic data on PAH:H₂O photoproducts are largely lacking in the literature, analysis of the non-volatile photoproducts after warm-up (i.e. thermal processing) has shown that the O, OH and H additions to the parent PAH are the dominant reaction pathways ([Ashbourn et al. 2007](#); [Bernstein et al. 1999, 2002](#)). Aromatic alcohols are among the known photoproducts, and the C–O stretching vibration in alcohols and phenols produces a strong band in the 1260–1000 cm^{-1} region (e.g., [Silverstein & Bassler 1967](#)). Additionally, the alcohol OH wag falls in the 1420 to 1330 cm^{-1} region. Besides alcohols, aromatic ketones are also amongst the photoproducts. The C=O stretch vibration in ketones typically occurs at around 1700 cm^{-1} . Keeping this in mind, tentative identifications of unassigned bands, i.e. not due to PAH⁺, are made below.

4.1.1. Anthracene:H₂O photoproducts

While most of the bands in the spectrum of the Ant:H₂O photoproducts can be attributed to Ant⁺, some prominent bands cannot. Two such bands appear at 1156 and 1243 cm^{-1} . It is possible that both of these absorptions originate from the CO stretch of two different Ant–OH isomers. The 1243 cm^{-1} band was previously attributed to an unknown Ant:H₂O photoproduct ([Bernstein et al. 2007](#)). Another prominent band that is not solely due to Ant⁺ occurs at 1452 cm^{-1} . While a small

Table 2. The band positions and relative integrated absorbances for the studied PAHs in H₂O ice at 15 K, and in an argon matrix at 10 K, as well as band positions computed using DFT.

PAH	Position (cm ⁻¹)			Relative I.A.		A _{band} ^a	
	H ₂ O	Ar	Theory ^b	H ₂ O	Ar	H ₂ O	
Ant	1001.7	1000.9	1000.7	0.7	0.8	6.8	
	1103.8			0.1		0.8	
	1127.4			0.2		1.9	
	1149.7	1149.2	1156.2	0.9	0.7	9.0	
			1157.7				
	1168.2	1166.9	1169.3	0.6	0.5	6.2	
	1186.8			0.1		1.0	
	1272.3	1272.5	1274.6	0.5	0.6	5.7	
	1316.0	1318.1	1311.2	1.0	1.0	10.4	
	1328.3			0.2		2.1	
	1347.7	1345.6,1346.4	1342.6	0.3	0.2	3.5	
	1400.1			0.3		3.1	
	1450.9	1450.5	1455.3	1.4	0.4	14.6	
		1460.0	1456.1		0.3		
	1537.9	1542.0	1533.7	0.8	0.8	8.7	
	1563.1			0.1		0.8	
		1610.5	1620.0		0.2		
	1624.4	1627.8		0.8	0.4	7.9	
	Py	1065.5			0.1		2.8
1096.4		1097.3	1092.3	0.2	0.2	5.1	
1136.6				0.1		2.1	
1176.3		1164.5	1160.8	0.3	0.1	6.1	
1185.6		1183.9	1188.3	1.0	1.0	21.7	
1244.0		1243.0	1253.1	0.5	0.2	10.3	
1313.7		1312.1	1314.6	0.2	0.2	5.3	
1435.1		1434.8	1427.0	0.8	0.6	17.3	
			1427.5				
1452.0				0.1		2.8	
1468.4		1471.0	1476.2	0.1	0.1	1.8	
1488.4				0.2		3.3	
1594.1			1586.1	0.6		12.7	
1600.5		1604.0	1597.0	0.6	0.4	12.0	
B _{ghi} P		1038.3	1036.3	1037.6	0.2	0.1	4.4
		1085.9	1087.8	1082.2	0.2	0.0	3.6
			1093.4	1091.9		0.0	
		1132.0	1132.7	1136.6	0.4	0.3	8.5
		1148.0	1149.2	1152.7	0.8	0.1	17.8
	1186.5	1186.9	1171.1	0.3	0.0	6.2	
			1206.6				
	1203.5	1206.7	1203.3	0.5	0.3	10.8	
	1258.7	1259.1	1261.5	0.1	0.0	1.7	
			1309.0				
	1305.6	1302.9,1307.0	1292.3	0.7	0.3	15.8	
	1334.6		1338.6	0.3		6.3	
	1342.2	1342.6	1336.0	1.0	1.0	22.5	
	1374.9	1350.0	1375.8	0.1	0.2	1.6	
			1398.9				
	1392.8	1394.7	1397.8	0.5	0.4	11.7	
	1414.8	1416.0,1417.1	1426.2	0.5	0.3	11.4	
	1447.8	1449.0,1451.1	1441.3	0.8	0.6	17.8	
	1479.7			0.2		4.7	
1512.8	1517.8	1513.3	0.2	0.0	3.5		
	1527.4			0.1			
1582.8	1602.1	1586.4	0.4	0.2	9.1		
1598.5		1586.6	0.3		6.5		
1614.7			0.1		1.3		
1618.9			0.1		2.4		

Notes. ^(a) The absolute intensities (A_{band}) for the PAHs in H₂O ice are in units 10⁻¹⁹ cm/molecule. ^(b) Values taken from: Langhoff (1996).

cation band is present near this position in the argon matrix data, it is much less intense with respect to the other cation bands whereas the photoproduct band in trace (E) (Fig. 2) is one of the strongest in the spectrum. This band is likely a blend of the cation band with a much stronger product band. The absorption frequency suggests that it originates from an aromatic CC stretching and C–H in-plane bending mode. Two strong photoproduct bands also appear in the blue end of the ROI, one at 1518 cm⁻¹, the other at 1604 cm⁻¹. The moderately strong Ant⁺ band at 1586.4 cm⁻¹ is expected to contribute to the blue end of the 1604 cm⁻¹ feature, but again seems to be too weak to explain

the full feature. Both the 1518 cm⁻¹ and most of the 1604 cm⁻¹ bands are likely due to the aromatic CC stretch vibration of a newly formed species.

The detection of new bands in the 1260–1000 cm⁻¹ region upon VUV photolysis of an Ant:H₂O mixture does agree with earlier findings by Ashbourn et al. (2007), who detected 1-anthrol and 2-anthrol using HPLC in a VUV irradiated Ant:H₂O ice (>1:100) after warm-up to room temperature. They also reported the formation of 1,4-anthraquinone, 9,10-anthraquinone and 9-anthrone. Anthraquinones contain two C=O bonds, which typically absorb at a frequency of 1676 cm⁻¹ (Chumbalov et al. 1967). This band position is outside of our ROI and detection is hampered by the strong H₂O bending mode. The other species detected by Ashbourn et al. (2007), 9-anthrone, belongs to the group of ketones and is expected to exhibit a C=O absorption at ~1700 cm⁻¹. The formation of this species can also not be confirmed for the same reason.

4.1.2. Pyrene:H₂O photoproducts

In the Py:H₂O case, the spectra in Fig. 2, trace (E) and photoproduct peak positions listed in Table 3 show that less than half of the new bands can be confidently assigned to Py⁺. As discussed above for Ant, the new features between 1260 and 1000 cm⁻¹ may be due to the CO stretch in various Py–OH isomers. Likewise, the prominent features at 1373 and 1393 cm⁻¹ can be tentatively attributed to modes involving both aromatic CC stretch and C–H in-plane bends of new products. The large number of photoproduct bands between 1500 and 1650 cm⁻¹ is striking, especially since only that at 1553 cm⁻¹ can be confidently attributed to Py⁺ based on matrix isolation spectra.

An attempt has been made to assign the unknown absorptions to more complex Py related species. Peak positions in the Py:H₂O photolysis experiments are compared to peak positions of 43 pyrene related species from the extensive theoretical database of PAH derivatives (Bauschlicher et al. 2010, www.astrochem.org/pahdb). Some groups of molecules indeed do exhibit strong transitions around the peak positions where the absorption maxima are found for the undefined Py:H₂O photoproducts. These molecules include H, OH, and O added pyrene-based species, such as C₁₆H₁₁O, C₁₆H₁₀O, C₁₆H₁₂, and their cations, in a variety of possible configurations. Although some of these theoretical peak positions overlap with the photoproduct bands, accurate experimental spectral data for these molecules are needed for unambiguous identifications of the reaction products of Py in VUV photolyzed H₂O ice.

4.1.3. Benzo[ghi]perylene:H₂O photoproducts

As molecular size increases, the number of mid-IR transitions grows and, because of spectral congestion, subtraction of neutral precursor bands becomes increasingly difficult. This makes it hard to obtain clear-cut spectra of the products in the B_{ghi}P photoprocessed ice and hence makes identification of individual bands difficult, if not impossible. As with Ant and Py, the spectra in Fig. 2 and photoproducts listed in Table 3 show that several absorption bands appear which clearly do not have a matrix cation counterband. Unassigned absorptions are found between 1470 and 1540 cm⁻¹ and probably involve CC stretching and C–H in plane bending modes. The strong unidentified bands between 1600 and 1640 cm⁻¹ are likely caused by the C=O stretching mode of B_{ghi}P ketones formed in the ice.

Table 3. Band positions of photoproducts appearing upon VUV photolysis of the studied PAHs in H₂O ice at 15 K compared to cation absorption band positions and band strengths measured in an argon matrix.

PAH	Position (cm ⁻¹)	Position ^a (cm ⁻¹)	Band strength ^{a,b}	Ass. ^c
	H ₂ O	Argon		
Ant	1155.7			
	1190.5	1183.3	0.37	+
		1188.6	18	+
	1242.7			
	1292.8	1290.4	1.5	+
	1326.2	1314.6	1.5	+
	1340.5	1341	26	+
	1358.3	1352.6	8.0	+
		1364.4	1.0	+
	1412.1	1406.1	0.39	+
		1409.5	2.7	+
	1419.5	1418.4	22	+
	1424.7	1430.2	0.38	+
	1452.2			
	1459.6	1456.5	1.9	+
	1517.9			
	1541.0	1539.9	3.9	+
	1567.2			
	1589.3	1586.4	3.6	+
	1603.6			
1621.1				
Py	1137.3			
	1182.0	1188.7	0.56	+
	1205.2			
	1216.7	1216.0	1.7	+
	1232.2			
	1247.6	1245.1, 1253.7, 1255.7	5.6	+
	1295.4			
	1319.0			
	1337.7			
	1359.0	1356.1, 1358.4, 1361.8	16	+
	1372.8			
	1393.2			
	1422.2	1421.1	2.3	+
	1446.0	1440.3	1.5	+
	1484.0			
	1537.5			
	1553.4	1550.9, 1553.4, 1556.0	13	+
	1567.4			
	1586.4			
	1614.0			
B _{ghi} P	1080.2			
	1126.4			
	1146.7	1140.2	5.5	+
	1191.0			
	1223.6	1216.7	0.46	+
		1223.4	4.1	+
	1253.1			
	1303.0			
	1322.9	1311.9	1.9	+
		1324.4	10	+
	1339.8	1331.9	2.3	+
	1346.2			
	1352.9	1350.2	2.1	+
	1366.8	1369.0	8.6	+
	1380.3			
	1388.4	1388.3	0.44	+
	1406.1	1401.3	12	+
		1408.8	0.64	+
	1433.3	1429.4	1.3	+
	1479.7			
1501.0				
1510.4				
1529.7				
1550.5	1538.6	0.25	+	
	1550.1	3.1	+	
1568.0				
1578.0	1578.2	14	+	
1590.2				
1604.7				
1617.0				
1624.3				

Notes. ^(a) Values taken from: [Hudgins & Allamandola \(1995a,b\)](#).

^(b) Band strengths are in units of 10⁻¹⁸ cm/molecule. ^(c) Cation bands are marked with a “+”.

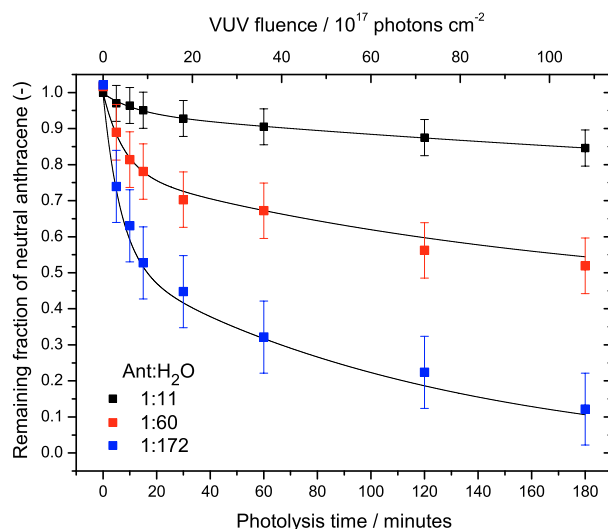


Fig. 3. Neutral anthracene decay as a function of photolysis time (VUV fluence) and concentration for 1:11, 1:60, and 1:172 Ant:H₂O mixtures at 15 K. Conservative errors are ± 5 , ± 7 , and $\pm 10\%$, respectively, of the initial amount of deposited neutral species. Fits to the data based on a sum of two exponentials (solid lines) are indicated as well.

Keeping the types of photoproducts in the Ant and Py ices in mind, it is most likely that B_{ghi}P derivatives containing H, O, and OH groups are formed upon photolysis. As for the Ant:H₂O and Py:H₂O experiments, we cannot unambiguously assign the B_{ghi}P photoproduct absorption bands. The non-volatile residue of a VUV irradiated B_{ghi}P:H₂O (<1:800) ice shows the addition of O, OH and H to the neutral parent ([Bernstein et al. 1999](#)). Thus, as with the other PAH:H₂O systems studied to date, it is likely that many of these new bands in the mid-IR are due to various forms of B_{ghi}P(-OH)_n, B_{ghi}P(=O)_n, and B_{ghi}P-H_n and possibly their ionized counterparts.

4.2. Concentration effects and time dependent chemistry

PAH:H₂O photolysis experiments have been performed for a set of concentrations ranging from ~1:11 to 1:200. Here only the Ant:H₂O experiments are described, but all three investigated PAHs exhibit a similar behavior. Figure 3 shows the decay in the amount of the neutral parent Ant in the ice as a function of photolysis time relative to the amount of the freshly deposited Ant before irradiation. Clearly, Ant loss is far more efficient for lower than for higher PAH concentration. Extrapolating these results, they are in good agreement with recent results that are described in Paper II ([Bouwman et al. 2010a, in prep.](#)) for PAH:H₂O ices at very low concentration (1:~5000 to 10000), where it was found that all the neutral PAH was consumed at the end of a 4 h photolysis experiment.

The 15 K neutral Ant decay data in Fig. 3 are co-plotted with a fit of the form $\Psi = C_1 \exp(-t/\tau_1) + C_2 \exp(-t/\tau_2)$. Fitting the experimental data required a sum of two exponentials. This indicates that more than one process is responsible for the neutral Ant loss. This is consistent with the optical work reported by [Bouwman et al. \(2010b, in prep.\)](#) in which two photochemical reaction networks were described, one for PAH cation formation, the other involving H, O, and OH PAH addition reactions.

The time dependent PAH cation and other photoproduct signals are also studied as a function of photolysis time (VUV dose). For the lowest concentration Py:H₂O ice in our sample (1:200), the time dependent behavior of the photoproduct

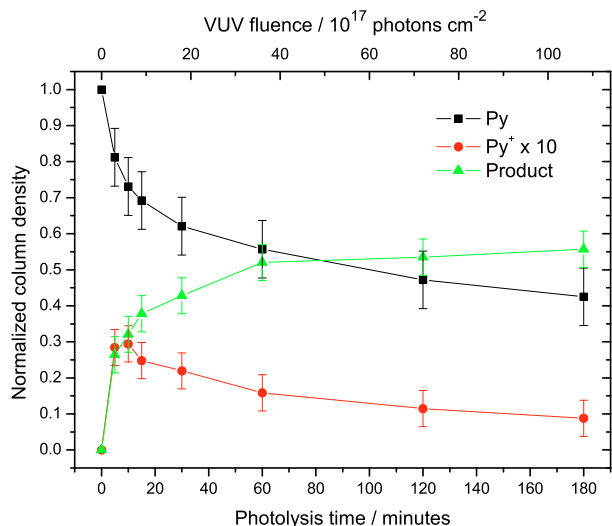


Fig. 4. Evolution of Py, Py^+ and a single Py photoproduct for a 1:200 Py: H_2O ice at 15 K as a function of photolysis time (VUV fluence). Photoproduct species are tracked using the 1359 and 1553 cm^{-1} Py^+ and 1567 cm^{-1} Py photoproduct bands.

bands is compared to the optical results presented in Paper II. To this end, the behavior of the cation is traced as a function of VUV time by integrating two of the most isolated prominent Py^+ absorption bands in the spectra, located at 1359 and 1554 cm^{-1} . Figure 4 shows the time evolution of the column density of the Py^+ species derived from these bands (multiplied by a factor of 10 and normalized to the initial amount of neutral Py to facilitate the display) together with the time evolution of the relative amount of neutral Py in the ice based on the subtraction factor, Y . The photolytic behavior of the integrated absorption of the strongest undefined photoproduct band at 1567 cm^{-1} (multiplied by a factor of 100 to facilitate the display) is also shown. Because no information is available on the band strength of this species, we cannot convert this integrated absorbance into a column density relative to the amount of deposited neutral PAH. The Py^+ bands and 1567 cm^{-1} photoproduct band show a different time dependence and clearly do not correlate. While the integrated absorbance of Py^+ reaches a maximum after some 10 min and then declines, the photoproduct signal grows and levels off towards the end of the experiment.

The error in the Py^+ column density is reduced by taking the average column density based on the two strongest cation absorptions located at 1359 and 1554 cm^{-1} . We estimate the error in the relative Py^+ abundance to be $\pm 5\%$ of the deposited amount of neutral Py and, thus, the shape of the time dependence curve is well defined. The error in the absolute number, however, is much larger because the argon band strength values from Table 3 have to be used for the analysis and because of ill-defined baselines caused by spectral congestion. Therefore, the error in the absolute amount of Py^+ produced can be quite high. For this reason, reliable quantitative time dependent data can only be obtained in the optical spectral regime, where cation absorptions are isolated and spectra are taken on a much shorter time scale. This is described in Paper II of this series (Bouwman et al. 2010a, in prep.). The error in the absolute number of neutral Py molecules consumed, on the other hand, is low ($\pm 7\%$). Since no information is available on the band strength of the 1567 cm^{-1} unidentified photoproduct absorption band, no quantitative information can be obtained on the formation of the species responsible for this band.

Using the PAH cation in Ar band strengths values, it is also possible to derive F_{frac} , the first order estimate of the fraction of the used-up neutral PAH that is converted into cation species versus other photoproducts. The amount of deposited neutral, N_{PAH} , is known from concentration measurements (Eqs. (1) and (2)) and the amount of consumed neutral is given by $(1 - Y)N_{\text{PAH}}$. The cation column density, N_{PAH^+} , is calculated with Eq. (2) and the band strength values reported in Table 3. The difference between the two, $(1 - Y)N_{\text{PAH}} - N_{\text{PAH}^+}$, makes up the photoproduct column density. The fraction of consumed neutral PAH molecules converted into PAH^+ is given by:

$$F_{\text{frac}} = \frac{N_{\text{PAH}^+}}{[(1 - Y)N_{\text{PAH}}]} \quad (4)$$

Values F_{frac} have been derived for different conditions for the three PAHs studied here. After 5 min of VUV photolysis of the Py: H_2O (1:200) mixture, about 20% of the neutral pyrene is used up and of this fraction roughly 15% is converted into Py^+ and 85% in other charged and/or neutral photoproducts. The Py^+ absorption peaks at about 10 min of VUV photolysis, a value that is also found in the optical study for much lower PAH concentrations (1:5000–1:10000). A mid-IR experiment on an ice sample with a higher Py concentration (1:60) results in an even lower F_{frac} value of about 0.05, a trend that suggests that ionization is more important in low concentration ices. Similar trends are found for low concentration mixtures of $\text{B}_{\text{ghi}}\text{P}$ – a (1:160) mixture gives $F_{\text{frac}} \approx 0.20$ – and Ant – a (1:172) mixture gives $F_{\text{frac}} \approx 0.10$ – after 5 min of VUV photolysis.

The quantitative analysis by Bouwman et al. (2010b) points out that there is a $\text{Py}^+ + \text{e}^-$ recombination channel. It is argued that the recombination reaction is most likely a local process, i.e., the electron released after ionization remains in the vicinity of its parent Py molecule. Putting this in perspective with the data presented here, this means that the recombination channel can well be more efficient in ices of higher concentration; the chance of recombination with an electron released from a neighboring Py molecule is larger. In the higher concentration experiments presented here, not all the neutral PAH is used up. Presumably some of the deposited PAHs are shielded from VUV irradiation and therefore not ionized. This may also explain the difference between the ionized fraction in low versus high concentration ices. Furthermore, as discussed before, ionization seems to be less efficient at high concentration ices, because chemical reactions between PAHs and radical species likely dominate the loss of the neutral species.

In summary, all PAH molecules trapped in H_2O ice exhibit a similar photoprocessing behavior. Ionization is more important in low concentration ices. However, after 5 min of VUV photolysis, most of the destroyed neutral species are converted into different PAH based photoproducts other than the cation. The concentration of the ice sample has a large influence on the efficiency of the chemical reactions. PAHs in lower concentration ices are used up faster and more efficiently, whereas in higher concentration ices, the PAH consumption is far less efficient. Although no mid-IR VUV photolysis measurements have been performed on coronene: H_2O ice mixtures, the near-UV/VIS study presented in Paper II of this series (Bouwman et al. 2010a, in prep.) shows that also coronene exhibits a similar behavior.

4.3. Ionization efficiency in CO ice

A control experiment has been performed on a Py:CO ice sample at 15 K to investigate the ionization efficiency of PAHs upon

photolysis in a CO matrix. After a short photolysis time (150 s), the ice exhibits weak absorptions at 1861 and 1090 cm⁻¹. These mid-IR absorption bands were previously assigned to the HCO[•] radical by Milligan & Jacox (1969). This observation is consistent with experiments performed by Bouwman et al. (2010b), where the electronic HCO[•] signature is found in the 500 to 660 nm spectral range. There, it is also found that, in a CO matrix, the Py ionization efficiency is close to zero, unless a certain level of H₂O contamination in the CO matrix is reached. In the mid-IR experiment performed here, VUV photolysis of Py in a CO matrix indeed does not show any sign of pyrene ionization, but also does not show any other PAH:H₂O photoproduct bands. We do confirm the low ionization efficiency and the appearance of small HCO[•] absorptions in a nearly pure CO ice, but no absorptions caused by PyH[•] species, as in the optical study, are observed. The fact that PAH absorption band strengths typical of electronic transitions are 100 times stronger than those for vibrational transitions, and that the level of H₂O contamination, i.e. the source of H-atoms for the reaction H[•] + CO[•] → HCO[•], is lower in the experiments described here, probably explains why the PyH[•] mid IR absorption bands were not detected. The important conclusion that follows from this control experiment is that H₂O catalyzes the ionization process. This is also consistent with the observation that ionization seems to be more efficient in low concentration PAH:H₂O ices.

4.4. Temperature effects

VUV photolysis experiments on PAH:H₂O samples (~1:60) were also conducted at a higher temperature (125 K). Consistent with the behavior reported in the optical studies (Bouwman et al. 2010b), we find that the neutral PAH loss is still efficient, while the ionization channel is strongly suppressed. The less efficient formation of the cation can point to a lower rate of ionization, but it is also possible that the recombination channel becomes dominant at higher temperatures. The result is that, at higher temperatures, the parent PAHs are more efficiently converted into species other than the PAH cation.

In the high temperature Py:H₂O experiment, for example, some pronounced vibrational bands appear immediately upon VUV photolysis. These bands, located at 1137.8, 1216.7, 1386.1 cm⁻¹ and a broad feature consisting of bands at 1553.5, 1566.1, and 1583.1 cm⁻¹, become strongest after 5 min of photolysis and then subside. Only the bands at 1216.7 and 1553.5 cm⁻¹ are at positions of Py⁺ absorptions. The remaining bands are also apparent in the low temperature spectra, but shifted by up to 3 cm⁻¹ and, in the absence of many of the other bands, seem to be more pronounced in the high temperature photolysis dataset.

For the PAH:H₂O ices irradiated at high temperatures there is a very broad overlapping substructure superimposed on the baseline of their mid-IR spectra. This is presumably caused by blended photoproducts and possibly PAH aggregates. Together with the knowledge that more complex species have been detected in other experiments (Bernstein et al. 1999, 2002; Ashbourn et al. 2007), we conclude that predominantly a mixture of PAH-X_n species, with X being H, O, or OH, may have been formed and that only one or a few chemical reaction channels dominate, resulting in the observed bands.

Ices at a temperature of 125 K are known to be of different structure than ices at low temperature (Jenniskens & Blake 1994). This structural difference – amorphous at 15 K vs. cubic crystalline at 125 K – may explain the different photochemical behavior. However, Bouwman et al. (2010b) investigated the

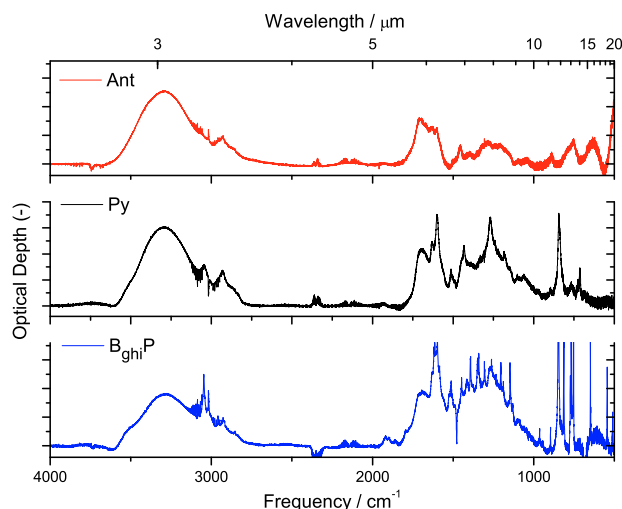


Fig. 5. Overview of the room temperature spectra of the residues accumulated during the photolysis of Ant, Py, and B_{ghi}P containing H₂O ices.

influence of the ice structure on the photoionization and found that ices annealed at 125 K and subsequently cooled down to 25 K exhibit similar ionization behavior as those grown and photolyzed at 25 K. Hence, they ascribed the different behavior at high temperatures to the larger mobility of radical species in the ice. The experiments presented here, point out a similar behavior.

5. The non-volatile residue

Figure 5 shows the 4000 to 500 cm⁻¹ room temperature spectra of the non-volatile residues produced by the photolysis of the three PAH:H₂O ices considered here. The spectra are measured as described in Sect. 2 and provide additional information on the photoproducts which have accumulated over a series of experiments for a particular PAH. These residues – complex mixtures of the non-volatile photoproducts, may also contain some of the parent PAH as well as some trapped H₂O or H₂O that accreted during the cooling of the sample window. Because the H₂O absorption bands in these spectra are much smaller than in the experiments on PAH:H₂O ice mixtures, the spectra can be investigated over the full range from 4000 to 500 cm⁻¹. In the ROI, the spectra show continuous, undulating absorptions from about 1750 to 1130 cm⁻¹ with several distinct features superposed. Additional spectral features are found between 3750 and 2750 cm⁻¹. The chemical subgroups indicated by these features are consistent with the addition of O, H, and OH to the parent PAH.

The aromatic-rich nature of these residues makes their spectra qualitatively different from the 13 residue spectra previously analyzed to compare with the spectrum of the diffuse interstellar medium (Pendleton & Allamandola 2002). While it is impossible to identify the molecules comprising the residues using infrared spectroscopy, it is possible to characterize the species and subgroups present by chemical type (i.e. aliphatic versus aromatic hydrocarbons, carbonyl vs. alcohol carbon-oxygen chemical bonds, etc.). The following analysis utilizes the characteristic group frequencies as well as relative and intrinsic band strengths as described in (Bellamy 1960; Silverstein & Bassler 1967; Wexler 1967). The prominent features in these spectra are discussed systematically from higher to lower frequency.

- *The 3300 cm⁻¹, O–H stretch:* a large part of this band can be ascribed to H₂O accretion to the cold sample, since the

residue spectra are based on background spectra taken of a cold sample window. However, the weak sideband near 3550 cm^{-1} points to the O–H stretching mode in phenols and, thus, the presence of aromatic alcohols in the residues.

- *The 3060 cm^{-1} aromatic C–H stretch*: the next prominent band, peaking near 3060 cm^{-1} , is due to the aromatic C–H stretch belonging to either the parent PAH or PAH photoproducts.
- *The $2990\text{--}2850\text{ cm}^{-1}$ aliphatic C–H stretch*: the addition of H to the aromatic parent forms a new type of functional group, which is evident from the broad aliphatic C–H stretch feature between about 2850 and 2990 cm^{-1} . The two subpeaks at about 2925 and 2860 cm^{-1} are characteristic of methylene ($-\text{CH}_2-$) groups, showing that the major H-addition channel proceeds by addition, not ring opening. If ring opening had been an important channel, bands due to the C–H stretches of methyl ($-\text{CH}_3$) groups near 2960 and 2870 cm^{-1} would have been expected. The assignment to methylene groups is further supported by the prominent band near $1450\text{--}1460\text{ cm}^{-1}$ in the lower two spectra shown in Fig. 5. A band in this region indicates the $-\text{CH}_2-$ scissoring mode in cyclic saturated compounds such as cyclohexane and cyclopentane. The spectrum of $\text{B}_{\text{ghi}}\text{P}$ is consistent with this analysis, but the bands are weaker. Given that the intrinsic strength of the aromatic C–H stretch is 10 times weaker than the intrinsic strength of the aliphatic C–H stretch per C–H (Wexler 1967), the increasing ratio of the aromatic band intensity to the aliphatic band intensity with PAH size indicates that H addition becomes less effective as the PAH size increases.
- *The 1700 cm^{-1} carbonyl C=O stretch*: as with the O–H stretching band near $3\text{ }\mu\text{m}$, some of this band may be attributed to the bending mode of H_2O molecules frozen onto the cold sample window. However, it is likely that part of this band is caused by the C=O stretch in carbonyl groups. In this case, quinone-like structures would be expected with the double bond to O participating in the conjugation of the molecule as a whole.
- *The band at 1625 cm^{-1}* : a distinct feature is evident at this frequency in all three spectra. The value is low for isolated carbonyls, but is characteristic for the carbonyl C=O stretch in molecules with intramolecular hydrogen bonding with an OH group.
- *The 1600 cm^{-1} aromatic CC stretch*: a well defined, but generally weak band centered near 1600 cm^{-1} is characteristic of the CC skeletal stretch in aromatic molecules. The prominence of this band in all three residue spectra shows, not surprisingly, that they are primarily aromatic in nature.
- *The bands between 1520 and 1500 cm^{-1}* : several features in this region become more prominent with parent PAH size. We are unable to attribute these bands to specific molecular vibrations.
- *The 1450 and 1440 cm^{-1} $-\text{CH}_2-$ scissoring vibration*: this band has been discussed in the paragraph describing the aliphatic C–H vibrations above.
- *The 1260 cm^{-1} band in the pyrene photoproduct*: while this prominent band falls in the $1300\text{--}1000\text{ cm}^{-1}$ region which is characteristic of aromatic C–H in-plane bending vibrations, other likely compounds also absorb in this region. For example, the C–O stretch in aromatic alcohols has a strong band between 1260 and 1180 cm^{-1} .
- *The 900 to 500 cm^{-1} aromatic C–H out-of-plane bends*: this region encompasses the very strong C–H out of plane vibrations which are diagnostic of substitution patterns on the

Table 4. Molecules, their vibrational modes and solid state absorption band positions possibly contributing to the $5\text{--}8\text{ }\mu\text{m}$ ice absorption complex towards low- and high-mass embedded objects.

Molecule	Mode	λ (μm)	ν (cm^{-1})	Ref.
H_2O	H–O–H bend	5.4–9	1852–1111	1
	Libr. overtone			1
H_2CO	C=O stretch	5.83	1715	2
CH_3HCO	C=O stretch	5.83	1715	3
HCOOH	C=O stretch	5.85	1709	3, 4
NH_3	H–N–H bend	6.16	1623	5
PAH?	CC stretch	6.20	1613	6
HCOO^-	C=O stretch	6.33	1580	3
H_2CO	H–C–H bend	6.68	1497	2
NH_4^+	Deformation	6.85	1460	7
HCOOH	C–H stretch	7.25	1379	3, 4
HCOO^-	C–H deform.	7.40	1351	3
SO_2	Asymm. stretch	7.58	1319	8
CH_4	Deformation	7.68	1302	9

References. (1) D’Hendecourt & Allamandola (1986); (2) Schutte et al. (1993); (3) Schutte et al. (1999); (4) Bisschop et al. (2007); (5) Kerkhof et al. (1999); (6) Keane et al. (2001), Kerkhof et al. (1999); (7) Schutte & Khanna (2003); (8) Boogert et al. (1997); (9) Boogert et al. (1996).

edge rings. In this case, these bands serve primarily as an indication of the presence of aromatic compounds.

All the pure PAHs under investigation here exhibit strong fluorescence upon excitation with a hand-held UV lamp. It is noteworthy, that after performing the experiments, the residues do not exhibit any fluorescence. This is consistent with the residues being processed PAHs with a different chemical identity.

6. Astrophysical implications

The $5\text{--}8\text{ }\mu\text{m}$ spectra of embedded low- and high-mass objects are generally dominated by two strong bands originating from interstellar ice, one centered near $6.0\text{ }\mu\text{m}$ and primarily attributed to the H_2O bending mode, and the other near $6.8\text{ }\mu\text{m}$. Close inspection of the spectra of many different molecular clouds shows that, while features near 6.0 and $6.8\text{ }\mu\text{m}$ are nearly always present, band positions, profiles, and relative strengths of other features vary somewhat from one object to another, revealing changes in ice composition and structure (e.g. Keane et al. 2001; Keane 2001; Gibb & Whittet 2002; Schutte & Khanna 2003; Boogert & Ehrenfreund 2004; Boogert et al. 2008). Besides the two dominant absorptions, signals are also found from other species that absorb in the $5\text{--}8\text{ }\mu\text{m}$ region. An overview of absorptions by molecular species in this wavelength region is given in Table 4. The knowledge of interstellar ice composition and chemistry is based on over twenty five years of dedicated studies on laboratory ice analogs to interpret these observations (see references mentioned above and Ehrenfreund & Charnley 2000; van Dishoeck 2004, and references therein). However, to date, such studies considering PAHs in ices and their contribution to the $5\text{--}8\text{ }\mu\text{m}$ absorption complex are lacking. Here, we discuss the possible contribution of PAHs in ices to the spectra of both high- and low-mass objects, using the laboratory data presented in the previous sections.

6.1. High-mass protostars

Figure 6 shows the $\sim 5.3\text{--}8.7\text{ }\mu\text{m}$ ($1900\text{--}1150\text{ cm}^{-1}$) ISO SWS spectrum towards the high-mass protostar W33A (based on data

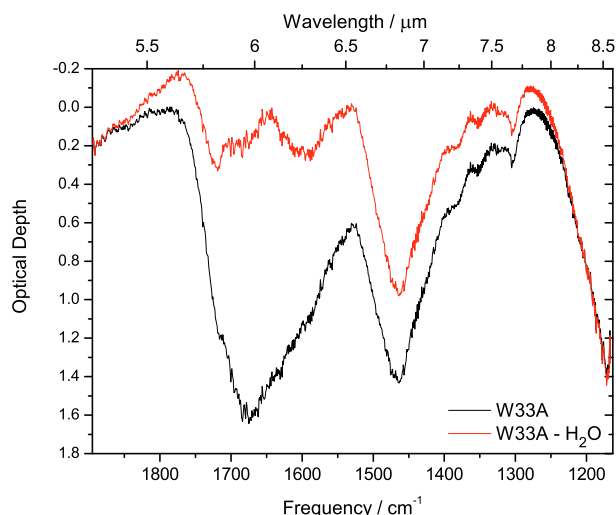


Fig. 6. The 5.3 to 8.7 μm ISO SWS spectrum of the high-mass protostar W33A plotted in optical depth together with the spectrum obtained after subtraction of the H₂O bending and librational overtone modes. The figure is adapted, with permission, from Keane et al. (2001).

from Keane et al. 2001) and the residual that remains after subtracting the H₂O bending and librational overtone bands in a manner similar to that described in Sect. 2. Based on a sample of five ISO spectra towards high-mass protostars, Keane et al. (2001) attributed the bulk of the 6.0 μm ice band to amorphous H₂O ice, with additional absorptions on the short wavelength wing near 5.8 μm and on the long wavelength wing near 6.2 μm . They assigned the short wavelength absorption at 5.83 μm to the carbonyl C=O stretch in formaldehyde and related species based on laboratory studies and suggested that the 6 μm long wavelength absorption at 6.2 μm can be due to the CC stretch of aromatic structures in PAHs or amorphous carbon particles. Keane et al. (2001) also showed that the 6.85 μm band is comprised of two components, one centered near 6.75 μm , and the other at 6.95 μm , but they did not assign possible band carriers. Noteworthy in Fig. 6 are also the weak undulating features between \sim 7.2 and 7.9 μm . Assignments of these absorption features are discussed in Schutte & Khanna (2003).

6.2. Low-mass protostars

Figure 7 shows the \sim 5.3–8.1 μm (1900–1234 cm^{-1}) spectrum of the low-mass YSO RNO 91, reproduced from Boogert et al. (2008) and the spectrum of the residuals that remain after subtracting the contribution by the water bending mode. In this more recent, extensive spectroscopic study of the 5–8 μm region of 41 low luminosity, low-mass protostars measured with the *Spitzer* telescope, Boogert et al. (2008) showed that, once the contribution from H₂O ice is removed, the 5–8 μm residual spectrum can be split into five components (C1–C5). The large sample of objects permitted Boogert et al. to extract rough band profiles, although not uniquely assignable to specific band carriers, and to determine source to source variations for all five components. The positions of the C1 through C4 components are similar to those described in Keane et al. (2001) and part of these bands can be attributed to the species mentioned in Table 4. C5, a very broad, underlying component that stretches from about 1725 to 1250 cm^{-1} (5.8–8 μm) cannot be explained by any of these species and is most likely a blend of more than one species. As

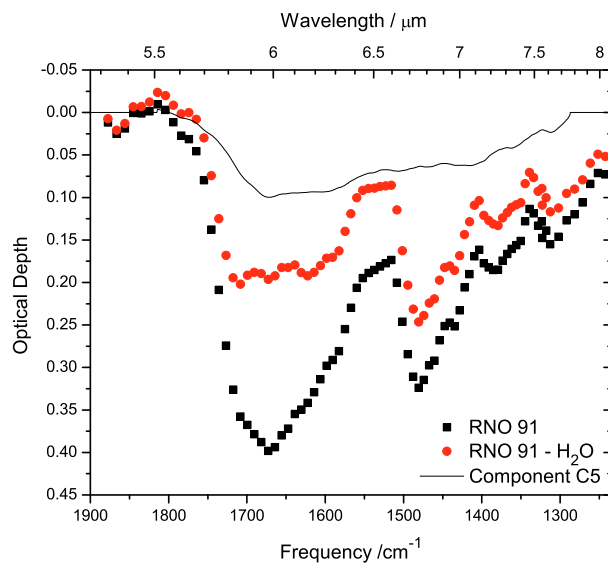


Fig. 7. The 5.3 to 8.1 μm *Spitzer* spectrum of the low-mass YSO RNO 91 plotted in optical depth together with the spectrum obtained after subtraction of the H₂O bending, and librational overtone modes. The C5 complex absorption as described by Boogert et al. (2008) is also indicated (solid line). The figure is adapted, with permission, from Boogert et al. (2008).

with the spectrum of W33A, RNO 91 also shows several weaker features between 7.2 and 7.9 μm .

6.3. PAH contributions to the 5–8 μm absorption

Here, we discuss the possible contribution that interstellar ices containing PAHs and their photoproducts could make to the spectra of molecular clouds in the 6.1–8.3 μm (1650–1200 cm^{-1}) region. The comparison is restricted to the three PAHs studied here. These three PAHs, Ant in particular, are on the low end of the PAH size distribution expected in space. As a consequence, the relative intensities of the modes are different than those expected for larger PAHs in the interstellar case. Infrared bands which result from the C–H functional group are expected to be less intense in space with respect to modes resulting from aromatic CC stretches, since astronomical PAHs are large and contain relatively more aromatic CC bonds than CH bonds. Figure 8 shows the photoproduct bands that appear after 180 min of VUV photolysis of the PAHs considered here in H₂O ice. All VUV processed PAH:H₂O mixtures under investigation exhibit bands clustered around 1600 cm^{-1} . The band at 6.2 μm , observed towards both low- and high-mass sources and also shown in Fig. 8, could well be caused by a superposition of many different large PAH and PAH photoproduct absorption bands, or organic refractory material as discussed in Sect. 5. Additional minor PAH absorptions throughout the 6–10 μm spectrum can be (partly) responsible for the underlying C5 complex absorption which is also indicated in Fig. 5 as well as the weak undulating structure between 7.2 and 7.9 μm .

The observational data also permit one to put crude limits on the column densities of PAHs condensed in interstellar ice. Assuming that the 6.2 μm feature in the residual spectra shown in Fig. 8 are due primarily to the aromatic CC stretching vibration in PAHs and closely related aromatic material frozen in H₂O-rich interstellar ice, one can estimate their column density (N_{PAH}) with Eq. (2). The integrated optical depths of the component are \sim 16 cm^{-1} for W33A and \sim 1.3 cm^{-1} for

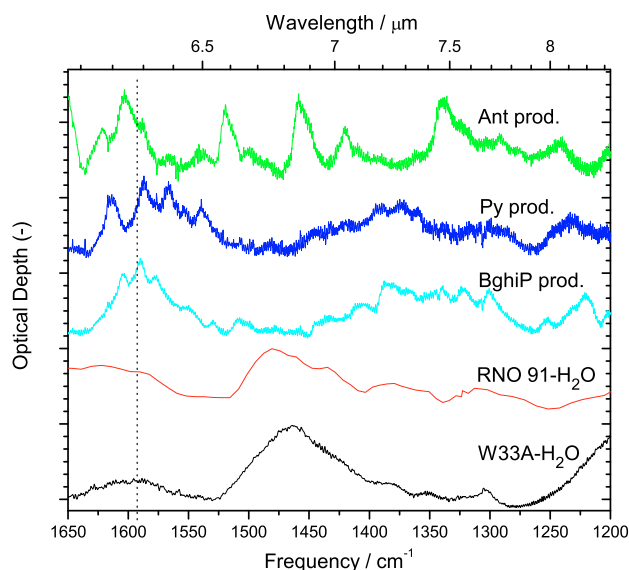


Fig. 8. The 6.1–8.3 μm (1650 cm^{-1} –1200 cm^{-1}) region of the spectra of W33A and RNO 91 after subtraction of the H_2O bending and librational overtone contributions plotted in absorbance compared to the spectra of the products after 180 min of PAH: H_2O ice photolysis. The dotted line guides the eye to the $\sim 6.2 \mu\text{m}$ ice absorption and main PAH: H_2O ice photoproduct bands.

RNO 91. The experimental data indicate that a certain number of neutral PAH species is converted into PAH photoproduct species, as indicated by $(1 - Y)N_{\text{neutral}}$, where N_{neutral} is the column density of deposited neutral molecules. This allows us to calculate an average band strength for the species responsible for the absorption band around $6.2 \mu\text{m}$ with Eq. (2). The resulting average band strength (A_{prod}) for the formed PAH products is $1.2 \times 10^{-17} \text{ cm molecule}^{-1}$. With these assumptions, the column density of neutral PAHs and PAH photoproducts frozen in H_2O is $1.3 \times 10^{18} \text{ molecules cm}^{-2}$ for the high-mass object (W33A) and $7.6 \times 10^{16} \text{ molecules cm}^{-2}$ for the low-mass object (RNO 91). Given that the column density of H_2O ice along the line of sight to these objects is $4 \times 10^{19} \text{ molecules/cm}^2$ and $4.3 \times 10^{18} \text{ molecules/cm}^2$ (Keane et al. 2001; Boogert et al. 2008), respectively, this implies PAH and PAH photoproduct abundances between 2–3% with respect to water. This concentration range is reasonable given the PAH abundances derived from mid-IR emission features (Puget & Leger 1989; Allamandola et al. 1989).

7. Conclusions

The manuscript describes mid-IR absorption spectroscopy of PAH: H_2O ices, their VUV induced photochemistry and photoproducts. The main conclusions of this manuscript are summarized below.

1. Band positions, *FWHMs*, and relative intensities of anthracene, pyrene and benz[ghi]perylene in H_2O ice in the 1650–1000 cm^{-1} spectral window are compared to their matrix isolation data. Additionally, band strengths are derived for these species isolated in an astrophysically relevant H_2O ice at 15 K.
2. VUV photolysis of PAH containing H_2O ice causes the embedded PAH to ionize and react with H_2O photoproducts. The band positions of PAH cations trapped in H_2O ice are measured and compared to PAH cation values from previous argon matrix isolation studies. Additionally, peak po-

sitions of PAH: H_2O photoproducts other than the cation are determined and tentatively assigned to PAH- X_n species, with X being O, H or OH.

3. The VUV induced photochemistry of the PAH pyrene in a CO ice was also studied. In this case, PAH ionization is inefficient compared to a VUV irradiated PAH: H_2O ice and seems to depend on the presence of trace amounts of H_2O .
4. The photochemistry is also tracked as a function of PAH: H_2O ice concentration for PAH: H_2O ratios $\sim 1:10$ to $1:200$. The fraction of neutral molecules converted into the cation is found to be larger in ices of lower concentration, consistent with the previous conclusion, whereas the fraction of neutral PAHs converted into photoproduct species other than the PAH cation is larger in ices of higher PAH concentration.
5. The PAH: H_2O ice photochemistry is tracked as a function of VUV fluence by monitoring the integrated absorbances of the parent PAH and PAH photoproduct bands periodically during photolysis for several hours. In all cases, the PAH cation bands peak after some 5 to 10 min and then slowly decline, while other photoproduct bands continue to grow steadily and starts to level off after about an hour of irradiation.
6. The ice photochemistry is monitored for two ice temperatures, 15 and 125 K. PAH cation formation is important and dominates the first few minutes in the low temperature case. However, ionization is far less efficient in the 125 K ice while the loss of the neutral parent PAH is equally efficient. It is concluded that reactions with H_2O photoproducts are the dominant channel at high temperatures.
7. Spectra from 4000 to 500 cm^{-1} of the non-volatile room temperature residue that builds up over the course of the experiments on each PAH species considered here are analyzed. These aromatic-rich residues contain OH, CO, and CH_2 groups as evidenced by absorptions in the OH stretching region (2.8 μm), CH stretching region (3.3–3.4 μm) and in the C=O, C–O, and aromatic CC region (5.6–10 μm).
8. The infrared data of the PAH photoproducts are compared to 5–8 μm ISO and *Spitzer* spectra of a high- and low-mass protostar. It is shown that PAH: H_2O ice photoproducts are plausible candidates for the 6.2 to 6.3 μm absorption band associated with interstellar ice and that these may contribute to some of the weak structure between about 6.9 to 8 μm . The band strength of the 6.2 to 6.3 μm band of the PAH: H_2O ice photoproducts reported here is determined. From this we derive an upper limit for interstellar abundance of PAHs and PAH: H_2O ice photoproducts with respect to H_2O ice of 2–3%.

Acknowledgements. The authors thank J. V. Keane (ISO-SWS, W33A) and A. C. A. Boogert (*Spitzer*, RNO 91) for placing the observational spectra at our disposal. This work is financially supported by NASA's Laboratory Astrophysics and Astrobiology Programs, "Stichting voor Fundamenteel Onderzoek der Materie" (FOM), and "the Netherlands Research School for Astronomy" (NOVA). J. Bouwman gratefully acknowledges the "Search for Extraterrestrial Intelligence" (SETI) institute for financial support. The research leading to these results has received funding from the [European Community's] Seventh Framework Programme [FP7/2007-2013] under grant agreement n° [238258].

References

- Allamandola, L. J., Tielens, A. G. G. M., & Barker, J. R. 1985, *ApJ*, 290, L25
 Allamandola, L. J., Tielens, A. G. G. M., & Barker, J. R. 1989, *ApJS*, 71, 733
 Andersson, S., & van Dishoeck, E. F. 2008, *A&A*, 491, 907
 Ashbourn, S. F. M., Elsila, J. E., Dworkin, J. P., et al. 2007, *Meteoritics and Planetary Science*, 42, 2035
 Bauschlicher, Jr., C. W., Peeters, E., & Allamandola, L. J. 2008, *ApJ*, 678, 316

- Bauschlicher, C. W., Peeters, E., & Allamandola, L. J. 2009, *ApJ*, 697, 311
 Bauschlicher, C. W., Boersma, C., Ricca, A., et al. 2010, *ApJS*, 189, 341
 Bellamy, L. J. 1960, *The Infra-Red Spectra of Complex Molecules* (Wiley)
 Bernstein, M. P., Sandford, S. A., Allamandola, L. J., et al. 1999, *Science*, 283, 1135
 Bernstein, M. P., Elsila, J. E., Dworkin, J. P., et al. 2002, *ApJ*, 576, 1115
 Bernstein, M. P., Mattioda, A. L., Sandford, S. A., & Hudgins, D. M. 2005a, *ApJ*, 626, 909
 Bernstein, M. P., Sandford, S. A., & Allamandola, L. J. 2005b, *ApJS*, 161, 53
 Bernstein, M. P., Sandford, S. A., Mattioda, A. L., & Allamandola, L. J. 2007, *ApJ*, 664, 1264
 Bisschop, S. E., Fuchs, G. W., Boogert, A. C. A., van Dishoeck, E. F., & Linnartz, H. 2007, *A&A*, 470, 749
 Boogert, A. C. A., & Ehrenfreund, P. 2004, in *Astrophysics of Dust*, ed. A. N. Witt, G. C. Clayton, & B. T. Draine, *ASP Conf. Ser.*, 309, 547
 Boogert, A. C. A., Schutte, W. A., Tielens, A. G. G. M., et al. 1996, *A&A*, 315, L377
 Boogert, A. C. A., Schutte, W. A., Helmich, F. P., Tielens, A. G. G. M., & Wooden, D. H. 1997, *A&A*, 317, 929
 Boogert, A. C. A., Pontoppidan, K. M., Knez, C., et al. 2008, *ApJ*, 678, 985
 Bouwman, J., Paardekooper, D. M., Cuppen, H. M., Linnartz, H., & Allamandola, L. J. 2009, *ApJ*, 700, 56
 Bouwman, J., Cuppen, H. M., Bakker, A., Allamandola, L. J., & Linnartz, H. 2010b, *A&A*, 511, A33
 Bregman, J. D., & Temi, P. 2001, *ApJ*, 554, 126
 Bregman, J. D., Hayward, T. L., & Sloan, G. C. 2000, *ApJ*, 544, L75
 Brooke, T. Y., Sellgren, K., & Geballe, T. R. 1999, *ApJ*, 517, 883
 Chiar, J. E., Tielens, A. G. G. M., Whittet, D. C. B., et al. 2000, *ApJ*, 537, 749
 Chumbalov, T. K., Chanysheva, I. S., & Muzychkina, R. A. 1967, *J. Appl. Spectroscopy*, 6, 570
 D'Hendecourt, L. B., & Allamandola, L. J. 1986, *A&AS*, 64, 453
 Draine, B. T., & Li, A. 2007, *ApJ*, 657, 810
 Ehrenfreund, P., & Charnley, S. B. 2000, *ARA&A*, 38, 427
 Gibb, E. L., & Whittet, D. C. B. 2002, *ApJ*, 566, L113
 Gudipati, M. S., & Allamandola, L. J. 2006, *ApJ*, 638, 286
 Hudgins, D. M., Sandford, S. A., Allamandola, L. J., & Tielens, A. G. G. M. 1993, *ApJS*, 86, 713
 Hudgins, D. M., Sandford, S. A., & Allamandola, L. J. 1994, *J. Phys. Chem.*, 98, 4243
 Hudgins, D. M., & Allamandola, L. J. 1995a, *J. Phys. Chem.*, 99, 3033
 Hudgins, D. M., & Allamandola, L. J. 1995b, *J. Phys. Chem.*, 99, 8978
 Hudgins, D. M., & Allamandola, L. J. 1997, *J. Phys. Chem. A*, 101, 3472
 Hudgins, D. M., & Sandford, S. A. 1998a, *J. Phys. Chem. A*, 102, 329
 Hudgins, D. M., & Sandford, S. A. 1998b, *J. Phys. Chem. A*, 102, 344
 Jenniskens, P., & Blake, D. F. 1994, *Science*, 265, 753
 Joblin, C., D'Hendecourt, L., Leger, A., & Defourneau, D. 1994, *A&A*, 281, 923
 Keane, J. V. 2001, Ph.D. Thesis, Rijksuniversiteit Groningen
 Keane, J. V., Tielens, A. G. G. M., Boogert, A. C. A., Schutte, W. A., & Whittet, D. C. B. 2001, *A&A*, 376, 254
 Kerkhof, O., Schutte, W. A., & Ehrenfreund, P. 1999, *A&A*, 346, 990
 Langhoff, S. R. 1996, *J. Phys. Chem.*, 100, 2819
 Li, A., & Draine, B. T. 2002, *ApJ*, 572, 232
 Mattioda, A. L., Allamandola, L. J., & Hudgins, D. M. 2005a, *ApJ*, 629, 1183
 Mattioda, A. L., Hudgins, D. M., Bauschlicher, C. W., & Allamandola, L. J. 2005b, *Adv. Space Res.*, 36, 156
 Milligan, D. E., & Jacox, M. E. 1969, *J. Chem. Phys.*, 51, 277
 Öberg, K. I., Linnartz, H., Visser, R., & van Dishoeck, E. F. 2009, *ApJ*, 693, 1209
 Peeters, E., Allamandola, L. J., Hudgins, D. M., Hony, S., & Tielens, A. G. G. M. 2004, in *Astrophysics of Dust*, ed. A. N. Witt, G. C. Clayton, & B. T. Draine, *ASP Conf. Ser.*, 309, 141
 Pendleton, Y. J., & Allamandola, L. J. 2002, *ApJS*, 138, 75
 Puget, J. L., & Leger, A. 1989, *ARA&A*, 27, 161
 Rapacioli, M., Calvo, F., Joblin, C., et al. 2006, *A&A*, 460, 519
 Sandford, S. A. 2002, *Planet. Space Sci.*, 50, 1145
 Sandford, S. A., & Allamandola, L. J. 1993, *ApJ*, 417, 815
 Sandford, S. A., Bernstein, M. P., & Allamandola, L. J. 2004, *ApJ*, 607, 346
 Schutte, W. A., Allamandola, L. J., & Sandford, S. A. 1993, *Science*, 259, 1143
 Schutte, W. A., Boogert, A. C. A., Tielens, A. G. G. M., et al. 1999, *A&A*, 343, 966
 Schutte, W. A., & Khanna, R. K. 2003, *A&A*, 398, 1049
 Sellgren, K., Brooke, T. Y., Smith, R. G., & Geballe, T. R. 1995, *ApJ*, 449, L69
 Silverstein, G. C., & Bassler, R. M. 1967, *Spectrometric Identification of Organic Compounds Second Edition* (Wiley)
 Smith, R. G., Sellgren, K., & Tokunaga, A. T. 1989, *ApJ*, 344, 413
 Smith, J. D. T., Draine, B. T., Dale, D. A., et al. 2007, *ApJ*, 656, 770
 Szczepanski, J., & Vala, M. 1993, *ApJ*, 414, 646
 Szczepanski, J., Chapo, C., & Vala, M. 1993a, *Chem. Phys. Lett.*, 205, 434
 Szczepanski, J., Vala, M., Talbi, D., Parisel, O., & Ellinger, Y. 1993b, *J. Chem. Phys.*, 98, 4494
 Szczepanski, J., Drawdy, J., Wehlburg, C., & Vala, M. 1995a, *Chem. Phys. Lett.*, 245, 539
 Szczepanski, J., Wehlburg, C., & Vala, M. 1995b, *Chem. Phys. Lett.*, 232, 221
 Tielens, A. G. G. M. 2008, *ARA&A*, 46, 289
 van Dishoeck, E. F. 2004, *ARA&A*, 42, 119
 Wexler, A. 1967, *Appl. Spectroscopy Rev.*, 1, 29